ACS APPLIED MATERIALS & INTERFACES

Research Article

www.acsami.org

Role of Mn Content on the Electrochemical Properties of Nickel-Rich Layered $LiNi_{0.8-x}Co_{0.1}Mn_{0.1+x}O_2$ ($0.0 \leq x \leq 0.08$) Cathodes for Lithium-Ion Batteries

Jianming Zheng, Wang Hay Kan, and Arumugam Manthiram*

Materials Science and Engineering Program and Texas Materials Institute, The University of Texas at Austin, Austin, Texas 78712, United States

Supporting Information

ABSTRACT: Ni-rich layered oxides (Ni content >60%) are promising cathode candidates for Li-ion batteries because of their high discharge capacity, high energy density, and low cost. However, fast capacity fading, poor thermal stability, and sensitivity to the ambient moisture still plague their mass application. In this work, we systematically investigate the effects of Mn content on the structure, morphology, electrochemical performance, and thermal stability of the Ni-rich cathode materials $LiNi_{0.8-x}Co_{0.1}Mn_{0.1+x}O_2$ ($0.0 \leq x \leq 0.08$). It is demonstrated that with the increase in Mn content and decrease in Ni content, the cycling stability of $LiNi_{0.8-x}Co_{0.1}Mn_{0.1+x}O_2$ to a cutoff charge voltage of 4.5 V is significantly improved. The high-Mn-content electrode $LiNi_{0.72}Co_{0.10}Mn_{0.18}O_2$ shows a capacity retention of 85.7% after 100 cycles at a 0.2 *C* rate at room temperature, much higher than those of the lower Mn-content samples $LiNi_{0.80}Co_{0.10}Mn_{0.10}O_2$ (64.0%) and $LiNi_{0.76}Co_{0.10}Mn_{0.14}O_2$ (72.9%). The improved capacity retention of the high-Mn-content electrode $LiNi_{0.72}Co_{0.10}Mn_{0.18}O_2$ is due to the stabilization of the electrode/electrolyte interface, as evidenced by the lower solid-electrolyte interphase (SEI) resistance and charge-transfer resistance. Furthermore, with the increase in Mn content and decrease in Ni content, the thermal stability of the Ni-rich cathode is also remarkably enhanced.

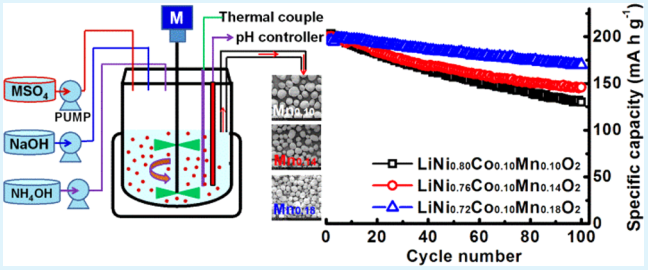

KEYWORDS: *lithium-ion batteries, manganese content, layered oxide cathodes, nickel-rich oxides, cycling stability, thermal stability*

INTRODUCTION

Besides serving as the power sources for portable electronic devices, lithium-ion batteries (LIBs) are being considered as one of the most promising candidates for the electric vehicles (EVs) and hybrid electric vehicles (HEVs).[1,2] However, further efforts are needed to improve the energy density, cycle life, and safety while lowering the cost for enabling long-range EVs. To date, lithium-rich layered oxides and nickel-rich layered oxides have been intensively investigated as high-energy density cathodes. Albeit the high discharge capacity (~250 mA h g^{-1}), significant challenges including voltage fade during cycling and limited cycle life exist with lithium-rich layered oxides.[3−7] Similarly, Ni-rich layered $LiNi_xCo_yMn_zO_2$ (NCM) cathodes with $x > 0.60$ and involving both the $Ni^{2+/3+}$ and $Ni^{3+/4+}$ couples offer capacities of 200−220 mA h g^{-1} but require high charge cutoff voltages of 4.5 V or above.[8−12]

Unfortunately, the high charge voltages result in a severe reaction of the nickel-rich surface with the electrolyte, formation of a thick solid-electrolyte interphase (SEI) layer, rapid increase in interfacial resistances, and fast capacity fade.[13−15] Furthermore, the formation of Li/O vacancies at deep charge at high voltages destabilizes the highly oxidized $Ni^{3+/4+}$ ions, resulting in cation migrations and formation of surface reconstruction layers (SRL) consisting of spinel-like and/or NiO-like rock-salt phases.[8,16] The increased formation of SRL considerably increases the kinetic barrier for lithium-ion diffusion, leading to power fade and capacity degradation. A lot of effort has been dedicated to enhancing the electrochemical performance of the Ni-rich cathode materials. Representative approaches include lattice doping,[17,18] surface modification,[8,19−23] tuning the material composition,[24−28] and smart design of core−shell or concentration gradient structures.[1,2,13,14,29] Among these approaches, incorporation of more Mn into the lattice is an effective way to significantly enhance the structural stability of Ni-rich cathodes, by mitigating the irreversible side reactions with the electrolyte in the presence of electrochemically inactive Mn^{4+} on the surface.[24−28] Another advantage of Mn substitution is the improvement in thermal stability at high temperatures and reduction in the cost of the Ni-rich cathode materials. However, previous research on understanding the effects of Mn substitution has mainly focused either on those with a charge cutoff voltage of only 4.3 V[24] or those with relatively lower Ni content (high Co content).[26]

Received: January 26, 2015
Accepted: March 10, 2015
Published: March 10, 2015

DOI: 10.1021/acsami.5b00788
ACS Appl. Mater. Interfaces 2015, 7, 6926−6934

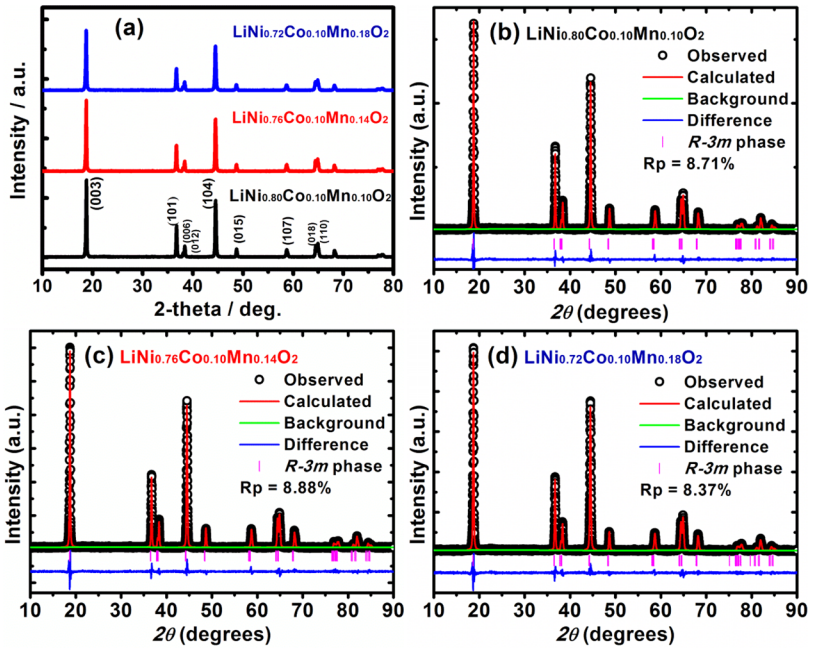

Figure 1. (a) XRD patterns of the $LiNi_{0.8-x}Co_{0.1}Mn_{0.1+x}O_2$ cathodes and the detailed Rietveld refinement results of (b) $LiNi_{0.80}Co_{0.10}Mn_{0.10}O_2$, (c) $LiNi_{0.76}Co_{0.10}Mn_{0.14}O_2$, and (d) $LiNi_{0.72}Co_{0.10}Mn_{0.18}O_2$.

With an aim to achieve a Ni-rich cathode material (Ni content >60%) with high energy density and improved cycling stability, we present here three Ni-rich layered $LiNi_{0.8-x}Co_{0.1}Mn_{0.1+x}O_2$ (x = 0, 0.04, and 0.08) cathodes with different Mn contents and spherical particles, synthesized by a continuous hydroxide coprecipitation method. To achieve high discharge capacity, these Ni-rich cathode materials are charged to a high cutoff voltage of 4.5 V. The effects of Mn substitution on the structure, morphology, electrochemical performance, and thermal stability of $LiNi_{0.8-x}Co_{0.1}Mn_{0.1+x}O_2$ cathode materials are investigated systematically. A more profound understanding of the positive effects of Mn content on Ni-rich cathode materials is presented.

EXPERIMENTAL SECTION

Material Preparation and Characterization. Spherical Ni-rich $Ni_{0.8-x}Co_{0.1}Mn_{0.1+x}(OH)_2$ precursors were prepared by a continuous hydroxide coprecipitation method, employing a continuously stirred tank reactor (CSTR) under N_2 atmosphere. Initially, the CSTR of 2 L capacity was filled with distilled water, which corresponds to 35% of the CSTR volume. Then, an aqueous solution consisting of $NiSO_4$, $CoSO_4$, and $MnSO_4$ with a concentration of 2.0 mol L^{-1} was continuously fed into the CSTR. At the same time, a NH_4OH solution as the chelating agent (10 mol L^{-1}) and NaOH solution (4.0 mol L^{-1}) were also separately pumped into the CSTR. The temperature (50 °C), stirring speed (1000 rpm), and pH value (pH = 11.5) were carefully controlled during the precipitation reaction in the CSTR. The precursor was filtered, thoroughly washed with distilled water, and dried overnight at 110 °C. $LiNi_{0.8-x}Co_{0.1}Mn_{0.1+x}O_2$ was prepared by thoroughly mixing the $Ni_{0.8-x}Co_{0.1}Mn_{0.1+x}(OH)_2$ precursor powder with LiOH, followed by calcining at 800 °C for 15 h in air. The heating and cooling rates were fixed at 3 °C min^{-1}. An excess amount of Li (3 mol %) was used to compensate the loss of Li during calcination at high temperatures.

Powder X-ray diffraction (XRD) of the synthesized samples was performed on a Rikagu MiniFlex 600 with Cu Kα radiation operated at 40 kV and 15 mA. Data were collected in the 2θ range of 10–90° at 3°/min. The lattice parameters were refined by the Rietveld method with the General Structure Analysis Software (GSAS program, Los Alamos National Laboratory). The refinements were carried out with the α-$NaFeO_2$-type hexagonal structure ($R\bar{3}m$) in which the Li^+ ions occupy the 3a (0, 0, 1/2) sites, Ni, Co, and Mn are located in the 3b (0, 0, 0) sites, and O is located in the 6c (0, 0, z_{oxy}) sites (z_{oxy} is close to 1/4). Scanning electron microscopy (SEM) studies were performed on a FEI Quanta 650 ESEM. Tap density was tested with an AUTOTAP tap density analyzer (Quantachrome Instruments). Surface area of the samples was determined with the Brunauer, Emmett, and Teller (BET) method using the nitrogen adsorption/desorption data collected with an Autosorb iQ gas sorption system (Quantachrome Instruments). The thermal stability of the $LiNi_{0.8-x}Co_{0.1}Mn_{0.1+x}O_2$ electrodes at a delithiated state of 4.5 V was examined with a differential scanning calorimetry (DSC, Netzsch STA 449F3 Jupiter thermal analysis system) from 30 to 350 °C at a heating rate of 10 °C min^{-1}.

Electrochemical Measurements. Electrochemical performance measurements were carried out with R2032 coin-type cells. Thin electrodes were prepared by coating a slurry mixture containing 80% active material, 10% super P, and 10% polyvinylidene fluoride (PVDF) binder (Kureha L#1120) onto an Al current collector foil. A typical loading of the thin electrodes is about 4–5 mg cm^{-2}. Thick electrodes with high areal capacity of 4 mA h cm^{-2} (~20 mg cm^{-2}) were prepared by coating a slurry mixture containing 90% active material, 5% super P, and 5% PVDF binder onto an Al current collector foil. After drying, the electrodes were punched into disks with an area of 1.13 cm^2. Electrochemical cells were assembled with the cathodes thus prepared, metallic lithium foil as counter electrode, Cellgard 2500 as separator, and 1 M $LiPF_6$ dissolved in ethyl carbonate (EC) and dimethyl carbonate (DEC) (1:1 in volume) as electrolyte in an argon-filled glovebox (Mbraun, Germany) in which both moisture and oxygen content were controlled below 1 ppm. Charge–discharge experiments were performed galvanostatically between 2.7 and 4.5 V on an Arbin BT-2000 battery tester at room temperature (~25 °C) and 55 °C. After the cell reached 4.5 V, an additional constant-voltage (CV) charging step at 4.5 V until the current rate reached 0.03 C was applied for charging the thick electrodes. The rate capability was evaluated with thin electrodes using a constant charge at C/5 and a gradual ascending in the discharge C rate after the initial five charge/discharge cycles at the C/5 rate. A 1 C rate corresponds to a current density of 200 mA g^{-1} in this work. Electrochemical impedance spectra (EIS) of the cells were collected at the charged state of 4.3 V at a frequency range from 100 000 to 0.01 Hz with a perturbation

DOI: 10.1021/acsami.5b00788
ACS Appl. Mater. Interfaces 2015, 7, 6926–6934

Table 1. Crystallographic Data Obtained from Rietveld Refinements, Tap Density, and BET Surface Area of $LiNi_{0.8-x}Co_{0.1}Mn_{0.1+x}O_2$

Ni-rich cathode	$LiNi_{0.80}Co_{0.10}Mn_{0.10}O_2$	$LiNi_{0.76}Co_{0.10}Mn_{0.14}O_2$	$LiNi_{0.72}Co_{0.10}Mn_{0.18}O_2$
a-axis (Å)	2.885(7)	2.887(1)	2.887(2)
c-axis (Å)	14.268(8)	14.274(4)	14.286(1)
unit volume (Å^3)	102.901	103.041	103.133
$I_{(003)}/I_{(104)}$	1.35	1.36	1.36
c/*a*	4.944	4.944	4.948
Ni in Li sites (%)	3.62	3.96	4.59
tap density (g cm^{-3})	2.13	2.10	2.10
BET surface area (m^2 g^{-1})	0.716	0.792	0.645

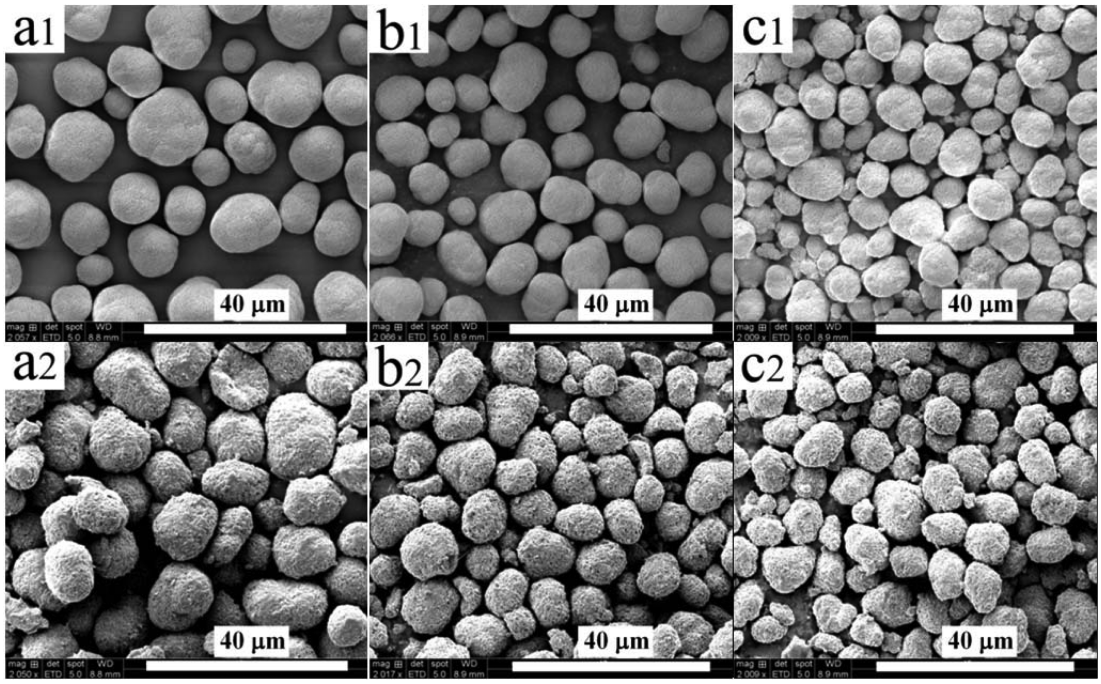

Figure 2. SEM images of the (a1−c1) $Ni_{0.8-x}Co_{0.1}Mn_{0.1+x}(OH)_2$ precursors and (a2−c2) lithiated $LiNi_{0.8-x}Co_{0.1}Mn_{0.1+x}O_2$ cathodes: (a1, a2) $x = 0$, (b1, b2) $x = 0.04$, and (c1, c2) $x = 0.08$.

amplitude of ±10 mV using a Solartron 1287 electrochemical interface coupled with 1260 frequency response analyzer.

RESULTS AND DISCUSSION

Figure 1 shows the XRD patterns and the refinement results of the Ni-rich layered $LiNi_{0.8-x}Co_{0.1}Mn_{0.1+x}O_2$. The XRD patterns in Figure 1a shows that the synthesized samples are all phase-pure without any impurity peaks detected. All the diffraction peaks of the XRD pattern could be indexed based on the layered hexagonal structure of α-$NaFeO_2$ belonging to the space group $R\bar{3}m$. The clear splitting between the (006) and (012) peaks as well as between the (018) and (110) peaks reveals a well-ordered layered structure of the samples. Rietveld refinement of the XRD data was carried out to obtain the lattice parameters and the cation disorder between Li and Ni, and the results are shown in Figure 1b−d and summarized in Table 1. The refinements all show good fit between the observed and calculated patterns, as presented in Figure 1b−d. The calculated lattice parameters, especially the *c* lattice parameter, increase with increasing Mn content. The lattice parameters of $LiNi_{0.80}Co_{0.10}Mn_{0.10}O_2$ are $a = 2.885(7)$ Å and $c = 14.268(8)$ Å, while those of of $LiNi_{0.72}Co_{0.10}Mn_{0.18}O_2$ are $a = 2.887(2)$ Å and $c = 14.286(1)$ Å. The increase in the lattice parameter is because of the substitution of the higher-valent Mn^{4+} ions for Ni^{3+} and the consequent reduction of a corresponding number of Ni^{3+} (0.60 Å) ions into larger Ni^{2+} (0.69 Å) ions to maintain charge neutrality.[24,26]

The degree of cation mixing between the lithium and nickel sites was also calculated with the assumption that some nickel ions may occupy the lithium sites because of the similar ionic radii of Ni^{2+} (0.69 Å) and Li^+ (0.76 Å). A slight increase in Li/Ni cation mixing was identified for the material with higher Mn content (Table 1). This is understandable because the increasing substitution of Mn^{4+} leads to the formation of more Ni^{2+} and facilitates cation mixing. In this regard, a compromise between improvement in cycle life/thermal stability with the introduction of Mn^{4+} and cation disorder should be considered in optimizing the Mn content. The intensity ratio ($I_{(003)}/I_{(104)}$) between the (003) and (104) diffraction peaks was analyzed to be ~1.35 for all the materials, further confirming a good layered structure of the materials.[30,31] The material $LiNi_{0.72}Co_{0.10}Mn_{0.18}O_2$ shows the highest $I_{(003)}/I_{(104)}$ and *c*/*a* ratio, signifying its superior electrochemical performances as compared to the other two samples.

SEM images of the $Ni_{0.8-x}Co_{0.1}Mn_{0.1+x}(OH)_2$ precursors and the lithiated $LiNi_{0.8-x}Co_{0.1}Mn_{0.1+x}O_2$ cathode materials are

DOI: 10.1021/acsami.5b00788
ACS Appl. Mater. Interfaces 2015, 7, 6926−6934

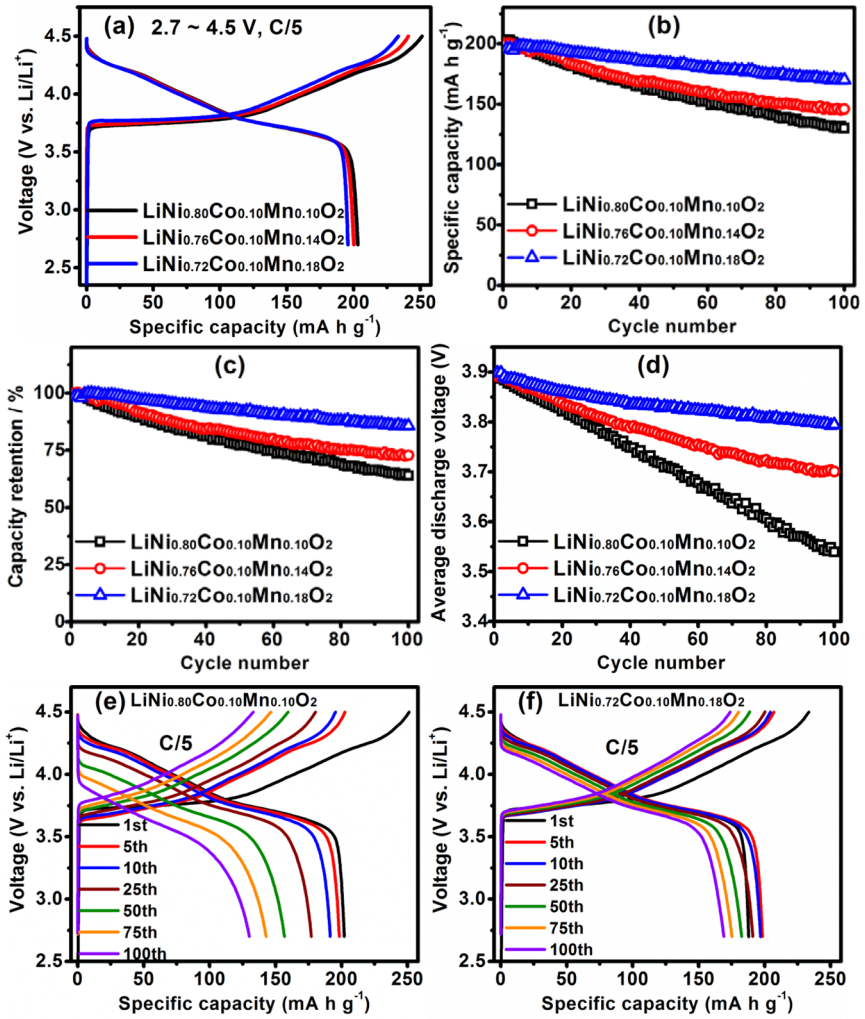

Figure 3. (a) Initial charge/discharge profiles, (b) cycling performance, (c) capacity retention, and (d) average discharge voltage of the $LiNi_{0.8-x}Co_{0.1}Mn_{0.1+x}O_2$ samples at *C*/5 over the voltage range of 2.7−4.5 V. Charge/discharge profile evolutions of (e) $LiNi_{0.80}Co_{0.10}Mn_{0.10}O_2$ and (f) $LiNi_{0.72}Co_{0.10}Mn_{0.18}O_2$ during cycling at the *C*/5 rate.

shown in Figure 2. All the precursors have a spherical particle size with an average particle size of about 10 μm in diameter. Small particles with 2−5 μm in diameter are also observed, which could be overcome if the continuous coprecipitation reaction is continued for a longer time by pumping more precursor reactants into the tank reactor. It is found that the precursor with higher Ni content, e.g., $Ni_{0.8}Co_{0.1}Mn_{0.1}(OH)_2$ shows slightly larger particles. With the increase in Mn content and decrease in Ni content, the precursors show reduced particle size and more small particles with a size of 2−5 μm are observed. This is because at the high pH value of 11.5, the Mn^{2+} ions with a weak coordination with ammonia easily precipitate out from the solution, leading to the formation of more small particles.[32] A slight decrease in the pH of the precipitation reaction could be an effective approach in our future work to enhance the coordination between Mn^{2+} and ammonia and thus facilitate the formation of larger spherical particles. After the high temperature calcination, the lithiated $LiNi_{0.8-x}Co_{0.1}Mn_{0.1+x}O_2$ cathode materials well inherited the spherical shape morphologies and average particle sizes of their spherical precursors, as shown in Figure 2a2−c2. The tap density of the three materials was determined to be ∼2.1 g cm^{-3} as listed in Table 1. One interest point is that the $LiNi_{0.72}Co_{0.10}Mn_{0.18}O_2$ sample shows tap density similar to $LiNi_{0.80}Co_{0.10}Mn_{0.10}O_2$, despite its smaller particle size. This result suggests that the spherical secondary particles in $LiNi_{0.72}Co_{0.10}Mn_{0.18}O_2$ are composed of more densely compacted primary particles, resulting in relatively smaller BET surface area as compared to the other two materials (see Table 1).

To evaluate the effects of Mn content on the electrochemical performances of $LiNi_{0.8-x}Co_{0.1}Mn_{0.1+x}O_2$, thin electrodes were first examined at room temperature with a charge cutoff voltage of 4.5 V at the *C*/5 rate and the results are shown in Figure 3. As presented in Figure 3a, the high-Mn-content cathode material shows a slightly higher charge voltage profile but exhibits a similar voltage profile during the discharge process. The material with higher Mn content shows lower charge capacity and thus a higher Coulombic efficiency in the first cycle, which is an indication of reduced side reactions between the high-Mn-content cathode and the electrolyte. The initial Coulombic efficiency increases from 80.9% for $LiNi_{0.80}Co_{0.10}Mn_{0.10}O_2$ to 83.9% for $LiNi_{0.72}Co_{0.10}Mn_{0.18}O_2$. At a *C*/5 rate, the initial discharge capacities are 203, 200, and 196 mA h g^{-1} for $LiNi_{0.80}Co_{0.10}Mn_{0.10}O_2$, $LiNi_{0.76}Co_{0.10}Mn_{0.14}O_2$, and $LiNi_{0.72}Co_{0.10}Mn_{0.18}O_2$, respectively. The capacity is slightly lower for the material with higher Mn content because of the

DOI: 10.1021/acsami.5b00788
ACS Appl. Mater. Interfaces 2015, 7, 6926−6934

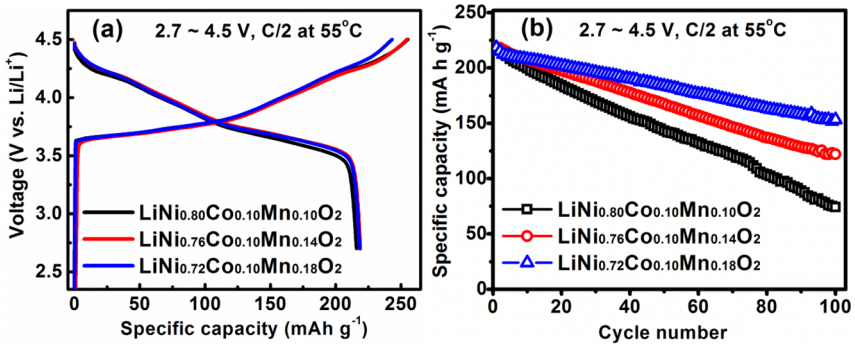

Figure 4. (a) Charge/discharge profiles and (b) cycling performance of the $LiNi_{0.8-x}Co_{0.1}Mn_{0.1+x}O_2$ materials at high temperature (55 °C) at the *C*/2 rate.

lowered content of electroactive Ni and the increased presence of electrochemical inactive Mn.

During cycling at the *C*/5 rate, noticeable differences are found in terms of discharge capacity as a function of cycle number and the capacity retention, as seen in Figure 3b,c. After 100 cycles, the high-Mn-content material $LiNi_{0.72}Co_{0.10}Mn_{0.18}O_2$ is still capable of delivering a high discharge capacity of 170 mA h g^{-1}, corresponding to a capacity retention of 85.7%, which is much higher than 64.0% and 72.9%, respectively, for $LiNi_{0.80}Co_{0.10}Mn_{0.10}O_2$ and $LiNi_{0.76}Co_{0.10}Mn_{0.14}O_2$ over the same cycling period (Figure 3c). Since the high-Ni-content sample shows the worst cyclability despite the least Li/Ni cation mixing, the main reason for the poor cycling stability of high-Ni-content material is attributed to the structural instability during repetitive charge/discharge processes. Because of the extensive lithium-ion removal and the possible release of oxygen at high voltages, the layered structure is destabilized and the migration of Ni ions to the neighboring Li layers becomes energetically favorable, which leads to a phase transformation from layered to spinel-like and/or disordered rock-salt structures, forming a surface reconstruction layer.[10,33−35] For the high-Ni-content material, e.g., $LiNi_{0.80}Co_{0.10}Mn_{0.10}O_2$, more Ni ions may migrate to the Li layers and a thicker surface reconstruction layer is expected due to presence of the high content of Ni at the particle surface. The migration of Ni into the Li layer (increase of cation mixing) during cycling drastically increases the kinetic barrier for the reversible lithium-ion de/intercalation, which largely increases the interfacial resistance and accelerates the capacity fading. With the decrease in Ni content and increase in Mn content, the electrochemically inactive Mn^{4+} plays an important role in stabilizing the material structure during extended electrochemical cycling. Thus, the material with lower Ni content and higher Mn content at the surface shows significantly enhanced cycling performance, despite its slightly higher cation disorder between Li and Ni before cycling. The result also implies that maintaining the structural stability during cycling is critically important to achieve good long-term cycling performance.

Because of the structural instability of Ni-rich materials, all of these materials show continuous voltage decay during cycling. The average discharge voltage of the $LiNi_{0.8-x}Co_{0.1}Mn_{0.1+x}O_2$ cathode materials with different Mn contents are shown in Figure 3d, while the charge/discharge voltage profile evolutions of $LiNi_{0.80}Co_{0.10}Mn_{0.10}O_2$ and $LiNi_{0.72}Co_{0.10}Mn_{0.18}O_2$ are further compared in Figure 3e,f. The apparent absence of voltage plateaus at around 4 or 3 V in the charge/discharge voltage profiles rules out the formation of real spinel-type phases before and after cycling. The data in Figure 3d−f demonstrate that the high-Mn-content material $LiNi_{0.72}Co_{0.10}Mn_{0.18}O_2$ exhibits the least voltage fade during cycling, which only shows a fade of 0.10 V after 100 cycles. This value is considerably lower than the voltage fades of 0.35 and 0.19 V for $LiNi_{0.80}Co_{0.10}Mn_{0.10}O_2$ and $LiNi_{0.76}Co_{0.10}Mn_{0.14}O_2$, respectively. The d*Q*/d*V* curves (Figure S1 in the Supporting Information) derived from the charge/discharge profiles in Figure 3e,f further demonstrate that the $LiNi_{0.80}Co_{0.10}Mn_{0.10}O_2$ electrode presents serious shrinkage in intensity and polarization of the redox reaction peaks, while the redox reaction peaks (position and intensity) are well maintained for the $LiNi_{0.72}Co_{0.10}Mn_{0.18}O_2$ electrode during cycling. The result further evidences the superior structural stability of the material with higher Mn content during cycling.

The electrochemical performance of the $LiNi_{0.8-x}Co_{0.1}Mn_{0.1+x}O_2$ cathode materials with different Mn content (thin electrode) were also evaluated at harsh testing conditions by charging to 4.5 V and cycling at *C*/2 at a high temperature of 55 °C, as shown in Figure 4. Significantly increased discharge capacities are seen for these Ni-rich cathode materials at 55 °C, which are 216, 219, and 218 mA h g^{-1}, respectively, for $LiNi_{0.80}Co_{0.10}Mn_{0.10}O_2$, $LiNi_{0.76}Co_{0.10}Mn_{0.14}O_2$, and $LiNi_{0.72}Co_{0.10}Mn_{0.18}O_2$, at the *C*/5 rate in the first cycle, suggesting an increase in electrode kinetics during charge/discharge at elevated temperatures. Lowered initial charge capacity is observed for the high-Mn-content material $LiNi_{0.72}Co_{0.10}Mn_{0.18}O_2$ (Figure 4a), again reflecting the mitigation of electrolyte oxidation upon charge to high voltages. It is worthy to note that the material with the highest Ni-content ($LiNi_{0.8}Co_{0.1}Mn_{0.1}O_2$) does not deliver the highest discharge capacity when discharging at 55 °C. This can be ascribed to the fact that the elevated temperature of 55 °C aggravates the structural instability of the high-Ni-content material, and the thicker surface reconstruction layer and SEI layer accumulated at the electrode surface considerably increase the kinetic barrier for the reversible lithium reintercalation even in the first cycle.

Although the low-Mn-content material $LiNi_{0.80}Co_{0.10}Mn_{0.10}O_2$ delivers high discharge capacity at the beginning, it shows fast capacity degradation during cycling with a low capacity retention of 34.3% after 100 cycles. A large decline in the voltage of the discharge profiles as well as a lowered discharge capacity is observed for $LiNi_{0.80}Co_{0.10}Mn_{0.10}O_2$ (Figure S2 in the Supporting Information). In contrast, the voltage of the discharge profiles and the

DOI: 10.1021/acsami.5b00788
ACS Appl. Mater. Interfaces 2015, 7, 6926−6934

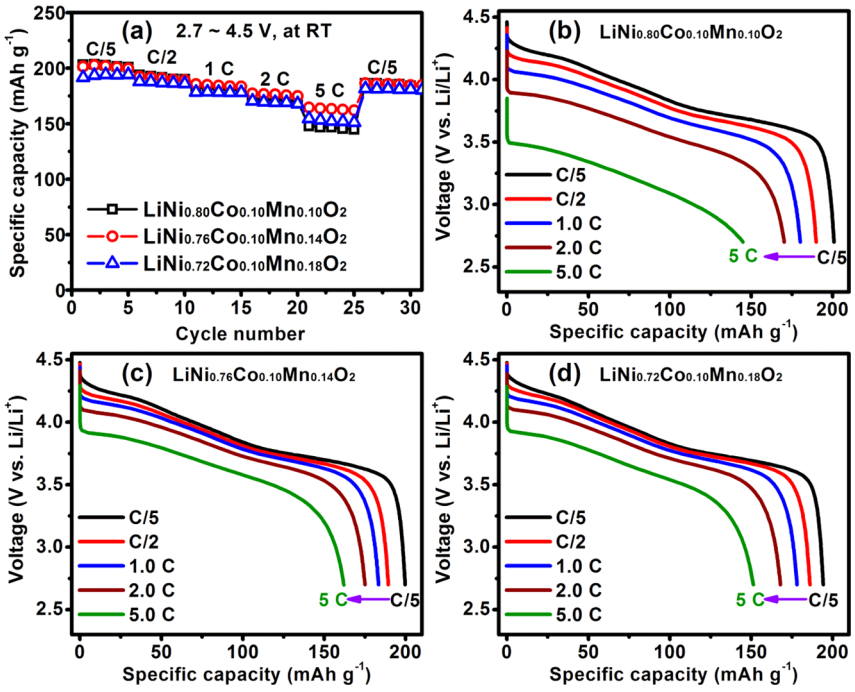

Figure 5. (a) Rate performance of the $LiNi_{0.8-x}Co_{0.1}Mn_{0.1+x}O_2$ materials at room temperature and the corresponding discharge profiles of (b) $LiNi_{0.80}Co_{0.10}Mn_{0.10}O_2$, (c) $LiNi_{0.76}Co_{0.10}Mn_{0.14}O_2$, and (d) $LiNi_{0.72}Co_{0.10}Mn_{0.18}O_2$ at different C rates in the voltage range of 2.7−4.5 V.

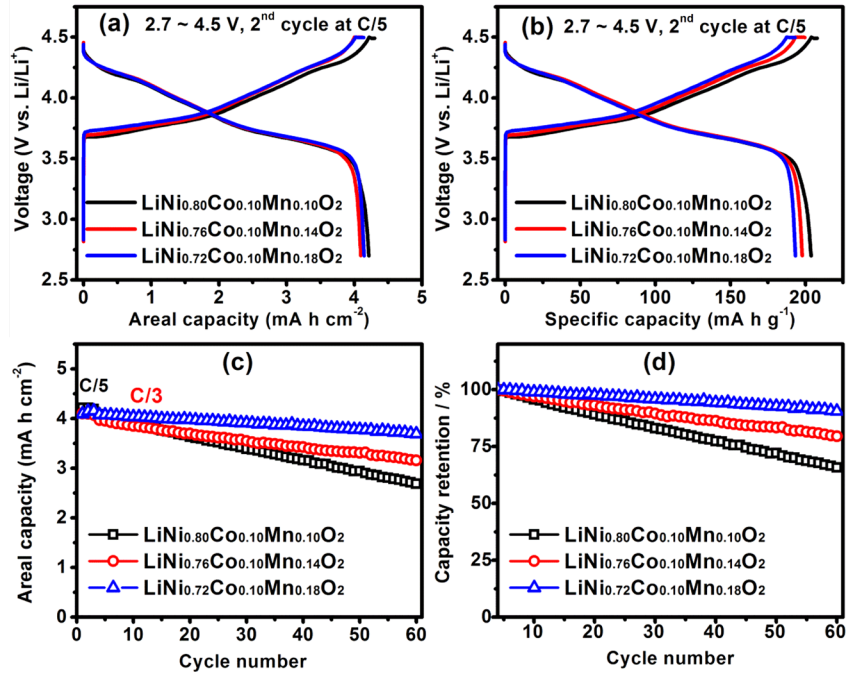

Figure 6. (a) Voltage profiles versus areal capacity, (b) voltage profiles versus specific capacity, (c) areal capacity as a function of cycle number, and (d) capacity retention of $LiNi_{0.8-x}Co_{0.10}Mn_{0.1+x}O_2$ samples with thick electrodes of about 20 mg of active material per cm^2.

discharge capacity are better maintained for the high-Mn-content $LiNi_{0.72}Co_{0.10}Mn_{0.18}O_2$. Consistent with the result obtained at room temperature, the material with higher Mn content presents remarkably improved cycling stability. The capacity retentions of $LiNi_{0.76}Co_{0.10}Mn_{0.14}O_2$ and $LiNi_{0.72}Co_{0.10}Mn_{0.18}O_2$ are improved to be 55.8% and 70.2% after 100 cycles, further validating the enhanced surface stability with the incorporation of higher Mn content.

Rate performances of the $LiNi_{0.8-x}Co_{0.1}Mn_{0.1+x}O_2$ cathodes with different Mn contents (thin electrode) are presented in Figure 5. The $LiNi_{0.76}Co_{0.10}Mn_{0.14}O_2$ sample shows higher discharge capacities at various C rates. In particular, the $LiNi_{0.76}Co_{0.10}Mn_{0.14}O_2$ sample shows the highest discharge capacity of 164 mA h g^{-1} at the 5C rate, which is much higher than the values of 148 and 155 mA h g^{-1} for $LiNi_{0.80}Co_{0.10}Mn_{0.10}O_2$ and $LiNi_{0.72}Co_{0.10}Mn_{0.18}O_2$, respectively. $LiNi_{0.72}Co_{0.10}Mn_{0.18}O_2$ shows a slightly poor rate capability as

DOI: 10.1021/acsami.5b00788
ACS Appl. Mater. Interfaces 2015, 7, 6926−6934

compared to $LiNi_{0.76}Co_{0.10}Mn_{0.14}O_2$, probably due to the reduced conductivity of the electrode because of the increase in Mn content. From the charge/discharge voltage profiles at different *C* rates, it can be found that the $LiNi_{0.80}Co_{0.10}Mn_{0.10}O_2$ sample shows discharge voltage profiles with dramatically reduced working voltage at elevated *C* rates (Figure 5b). This phenomenon indicates a significant increase in internal resistance and an obvious energy fade when discharging at increased current densities, which is undesirable for practical applications in power tools and electric vehicles. On the contrary, both $LiNi_{0.72}Co_{0.10}Mn_{0.18}O_2$ and $LiNi_{0.76}Co_{0.10}Mn_{0.14}O_2$ exhibit limited decay in the working voltage even at the 5*C* discharge rate, further confirming the improved structural stability and rate capability of materials with relatively higher Mn contents.

As high areal capacity of ~4 mA h cm^{-2} is required for practical applications, we also evaluated the electrochemical performance of these Ni-rich cathode materials $LiNi_{0.8-x}Co_{0.1}Mn_{0.1+x}O_2$ in thick electrode laminates with a loading of ~20 mg active material per cm^2, as shown in Figure 6a. The initial voltage profiles versus areal capacity of the $LiNi_{0.8-x}Co_{0.10}Mn_{0.1+x}O_2$ samples are shown in Figure S3 in the Supporting Information. The materials with higher Mn content shows a slightly higher cell polarization during the charge process, while exhibiting almost overlapped discharge profiles during the discharge process, suggesting that an activation process may be required for materials with higher Mn contents. After the first cycle, no obvious difference is observed in the charge and discharge profiles, as can be seen from Figure 6a,b. Thick $LiNi_{0.8-x}Co_{0.1}Mn_{0.1+x}O_2$ electrodes behave similarly to their thin-electrode counterparts and no evidence of capacity decrease is observed for electrodes with a high loading (20 mg cm^{-2}) as compared to those with a low loading of 4−5 mg cm^{-2} (Figure 6b). During cycling at the *C*/3 rate, the high-Mn-content cathode $LiNi_{0.72}Co_{0.10}Mn_{0.18}O_2$ shows superior cycling stability as compared to the other two samples. After 60 cycles, the capacity retention of $LiNi_{0.72}Co_{0.10}Mn_{0.18}O_2$ is 90.6%, remarkably higher than the values of 65.8% and 79.5% for $LiNi_{0.80}Co_{0.10}Mn_{0.10}O_2$ and $LiNi_{0.76}Co_{0.10}Mn_{0.14}O_2$, respectively. On the basis of the improved electrochemical performances of the high-Mn-content material $LiNi_{0.72}Co_{0.10}Mn_{0.18}O_2$ in electrodes with different loadings, it can be considered as a potential cathode candidate.

To get insight into the good structural stability of the material with high Mn content, electrochemical impedance spectroscopy (EIS) was carried out to study the interfacial electrochemistry and reaction kinetics of the $LiNi_{0.8-x}Co_{0.10}Mn_{0.1+x}O_2$ cathode materials in thick electrodes at the charged state of 4.3 V. The impedance spectra recorded at different stages of cycling are presented in Figure 7a,b, in which a high-frequency semicircle, an intermediate-frequency semicircle, and a low-frequency tail are observed. Generally, the high-frequency semicircle is related to the resistance arising from the passivation surface film (R_{sf}), the so-called SEI layer.[36,37] The intermediate-frequency semicircle is associated with the charge-transfer resistance (R_{ct}) in the electrode/electrolyte interface coupled with a double-layer capacitance. The low-frequency tail is associated with the Li^+ ion diffusion process in the active electrode particles.

The EIS spectra were fitted with the equivalent circuit[38,39] shown in Figure 8a, and the results are summarized in Figure 8b and detailed in Table S1 in the Supporting Information. Only a small difference is observed for the cells at early stages

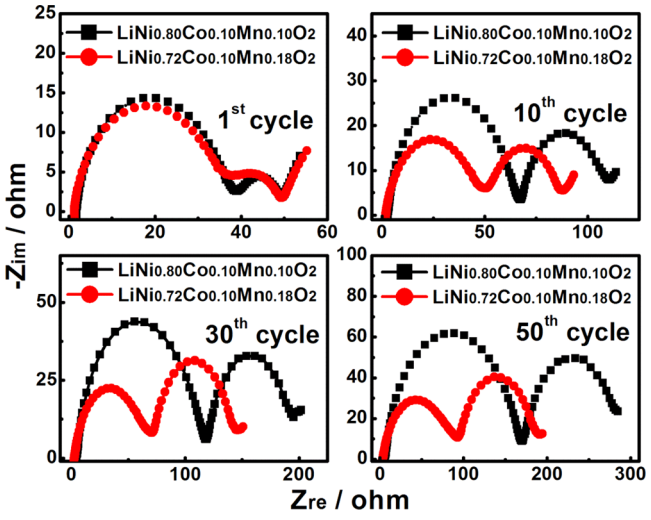

Figure 7. Nyquist plots of the $LiNi_{0.8-x}Co_{0.10}Mn_{0.1+x}O_2$ materials in thick electrodes at the charged state of 4.3 V during cycling at the *C*/3 rate after three formation cycles at the *C*/5 rate.

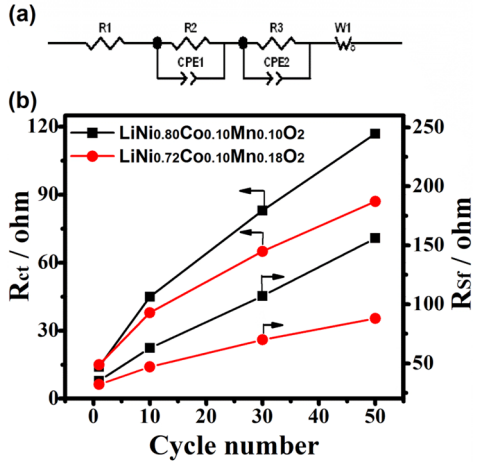

Figure 8. (a) Equivalent circuit used to fit the measured impedance spectra. (b) R_{ct} and R_{sf} as a function of cycle number for the $LiNi_{0.8-x}Co_{0.10}Mn_{0.1+x}O_2$ electrodes.

of cycling, exhibiting similar surface film resistance and charge-transfer resistance (Figure 8b). Upon cycling, the passivation surface-film resistance and the charge-transfer resistance of the high-Mn-content cathode $LiNi_{0.72}Co_{0.10}Mn_{0.18}O_2$ is considerably lower than those of the low-Mn-content cathode ($LiNi_{0.80}Co_{0.10}Mn_{0.10}O_2$), ascribed to the stabilization of the $LiNi_{0.72}Co_{0.10}Mn_{0.18}O_2$ electrode surface in the presence of the higher Mn content. After 50 cycles, $LiNi_{0.72}Co_{0.10}Mn_{0.18}O_2$ exhibits a low surface layer resistance (88 Ω), only about half that of the $LiNi_{0.80}Co_{0.10}Mn_{0.10}O_2$ electrode (156 Ω), indicating a thinner passivation film accumulated on the electrode surface. Meanwhile, the charge-transfer resistance of the $LiNi_{0.72}Co_{0.10}Mn_{0.18}O_2$ electrode (87 Ω) is also much smaller than that observed for the $LiNi_{0.80}Co_{0.10}Mn_{0.10}O_2$ electrode (117 Ω) over the same period of cycling. The stable interfacial resistances in the $LiNi_{0.72}Co_{0.10}Mn_{0.18}O_2$ electrode reflect an improved quality of electrode/electrolyte interface, which reversibly allows the timely charge transfer. It is believed that the reduced Ni content and increased Mn content at the particle surface of the $LiNi_{0.72}Co_{0.10}Mn_{0.18}O_2$ material is responsible for the interface stabilization during cycling,

DOI: 10.1021/acsami.5b00788
ACS Appl. Mater. Interfaces 2015, 7, 6926−6934

which is in good agreement with the electrochemical performance as discussed above.

To further understand the effect of Mn content on the thermal stability of the Ni-rich cathode materials, differential scanning calorimeter (DSC) plots of the $Li_{1-\delta}Ni_{0.80}Co_{0.10}Mn_{0.10}O_2$ and $Li_{1-\delta}Ni_{0.72}Co_{0.10}Mn_{0.18}O_2$ electrodes (thick electrode) were collected at the charged state of 4.5 V, as presented in Figure 9. The $Li_{1-\delta}Ni_{0.72}Co_{0.10}Mn_{0.18}O_2$

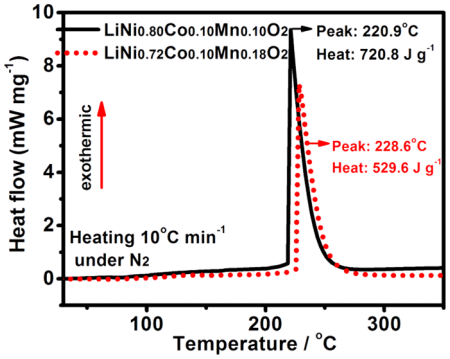

Figure 9. DSC profiles of the $Li_{1-\delta}Ni_{0.8-x}Co_{0.10}Mn_{0.1+x}O_2$ electrodes at the charged state of 4.5 V.

electrode exhibits an exothermic reaction with the peak located at 229 °C, which is much higher than the value of 221 °C for the $Li_{1-\delta}Ni_{0.80}Co_{0.10}Mn_{0.10}O_2$ electrode. Meanwhile, the exothermic heat generated from the thermal reactions between the $Li_{1-\delta}Ni_{0.72}Co_{0.10}Mn_{0.18}O_2$ electrode and the residual electrolyte is largely reduced to 527 J g^{-1}, as compared to 721 J g^{-1} for the $Li_{1-\delta}Ni_{0.80}Co_{0.10}Mn_{0.10}O_2$ electrode. The results suggest that increasing the Mn content and decreasing the Ni content in the Ni-rich cathode material, especially in the particle outer layer, significantly enhances the thermal stability of the Ni-rich cathode material.

CONCLUSIONS

The effects of Mn substitution for Ni on the structure, morphology, electrochemical performance at high charge cutoff voltage of 4.5 V, and thermal stability of the $Li-Ni_{0.8-x}Co_{0.1}Mn_{0.1+x}O_2$ ($0.0 \leq x \leq 0.08$) cathode materials have been investigated systematically. The findings highlight the importance of the surface structural stability of Ni-rich cathode materials, especially in the case of high charge cutoff voltages. Mn ions as incorporated into the Ni-rich cathodes, especially those existing at the particle surface, significantly reduce the irreversible side reactions between the electrode surface and the electrolyte and improve the surface structural stability. The sample with an optimized Mn-content ($LiNi_{0.72}Co_{0.10}Mn_{0.18}O_2$) shows significantly enhanced cyclability and reduced voltage decay during cycling, indicating a greatly improved structural stability and validating it as a promising cathode candidate. Considering the surface structural instability to electrolyte oxidation and phase transformation, additional surface coating with oxides such as TiO_2 or Al_2O_3 would be a facile approach to further enhance the surface structural stability of Ni-rich cathode materials and fully realize their practical applications in lithium-ion batteries. The findings of this work also shed light on the importance of developing concentration-gradient Ni-rich cathode materials with high Ni content in the bulk and high Mn content or high Mn content with some Al content in the surface.

ASSOCIATED CONTENT

Supporting Information

dQ/dV curve evolutions, charge/discharge profile evolutions at 55 °C, initial charge/discharge profiles of thick electrodes, and fitted results of EIS data of different cycles. This material is available free of charge via the Internet at http://pubs.acs.org.

AUTHOR INFORMATION

Corresponding Author

*E-mail: manth@austin.utexas.edu. Fax: +1-512-471-7681. Phone: +1-512-471-1791.

Author Contributions

The manuscript was written with contributions of all authors. All authors have given approval to the final version of the manuscript.

Notes

The authors declare no competing financial interest.

ACKNOWLEDGMENTS

This work was supported by the Assistant Secretary for Energy Efficiency and Renewable Energy, Office of Vehicle Technologies of the U.S. Department of Energy under Contract No. DE-EE0006447.

REFERENCES

(1) Sun, Y.-K.; Chen, Z.; Noh, H.-J.; Lee, D.-J.; Jung, H.-G.; Ren, Y.; Wang, S.; Yoon, C. S.; Myung, S.-T.; Amine, K. Nanostructured high-energy cathode materials for advanced lithium batteries. *Nat. Mater.* **2012**, *11*, 942−947.

(2) Sun, Y.-K.; Myung, S.-T.; Park, B.-C.; Prakash, J.; Belharouak, I.; Amine, K. High-energy cathode material for long-life and safe lithium batteries. *Nat. Mater.* **2009**, *8*, 320−324.

(3) Zheng, J.; Gu, M.; Genc, A.; Xiao, J.; Xu, P.; Chen, X.; Zhu, Z.; Zhao, W.; Pullan, L.; Wang, C.; Zhang, J.-G. Mitigating Voltage Fade in Cathode Materials by Improving the Atomic Level Uniformity of Elemental Distribution. *Nano Lett.* **2014**, *14*, 2628−2635.

(4) Zheng, J.; Gu, M.; Xiao, J.; Zuo, P.; Wang, C.; Zhang, J.-G. Corrosion/Fragmentation of Layered Composite Cathode and Related Capacity/Voltage Fading during Cycling Process. *Nano Lett.* **2013**, *13*, 3824−3830.

(5) Lee, E.-S.; Manthiram, A. Smart design of lithium-rich layered oxide cathode compositions with suppressed voltage decay. *J. Mater. Chem. A* **2014**, *2*, 3932−3939.

(6) Li, Q.; Li, G.; Fu, C.; Luo, D.; Fan, J.; Li, L. K^+-Doped $Li_{1.2}Mn_{0.54}Co_{0.13}Ni_{0.13}O_2$: A Novel Cathode Material with an Enhanced Cycling Stability for Lithium-Ion Batteries. *ACS Appl. Mater. Interfaces* **2014**, *6*, 10330−10341.

(7) Zhao, C.; Wang, X.; Liu, X.; Zhang, H.; Shen, Q. Mn−Ni Content-Dependent Structures and Electrochemical Behaviors of Serial $Li_{1.2}Ni_{0.13+x}Co_{0.13}Mn_{0.54-x}O_2$ as Lithium-Ion Battery Cathodes. *ACS Appl. Mater. Interfaces* **2014**, *6*, 2386−2392.

(8) Cho, Y.; Oh, P.; Cho, J. A New Type of Protective Surface Layer for High-Capacity Ni-Based Cathode Materials: Nanoscaled Surface Pillaring Layer. *Nano Lett.* **2013**, *13*, 1145−1152.

(9) Park, M.-H.; Noh, M.; Lee, S.; Ko, M.; Chae, S.; Sim, S.; Choi, S.; Kim, H.; Nam, H.; Park, S.; Cho, J. Flexible High-Energy Li-Ion Batteries with Fast-Charging Capability. *Nano Lett.* **2014**, *14*, 4083−4089.

(10) Jung, S.-K.; Gwon, H.; Hong, J.; Park, K.-Y.; Seo, D.-H.; Kim, H.; Hyun, J.; Yang, W.; Kang, K. Understanding the Degradation Mechanisms of $LiNi_{0.5}Co_{0.2}Mn_{0.3}O_2$ Cathode Material in Lithium Ion Batteries. *Adv. Energy Mater.* **2014**, *4*, DOI: 10.1002/aenm.201300787.

(11) Sun, Y.-K.; Lee, D.-J.; Lee, Y. J.; Chen, Z.; Myung, S.-T. Cobalt-Free Nickel Rich Layered Oxide Cathodes for Lithium-Ion Batteries. *ACS Appl. Mater. Interfaces* **2013**, *5*, 11434−11440.

DOI: 10.1021/acsami.5b00788
ACS Appl. Mater. Interfaces 2015, 7, 6926−6934

(12) Fu, C.; Li, G.; Luo, D.; Li, Q.; Fan, J.; Li, L. Nickel-Rich Layered Microspheres Cathodes: Lithium/Nickel Disordering and Electrochemical Performance. *ACS Appl. Mater. Interfaces* **2014**, *6*, 15822−15831.
(13) Yoon, S.-J.; Park, K.-J.; Lim, B.-B.; Yoon, C. S.; Sun, Y.-K. Improved Performances of $Li[Ni_{0.65}Co_{0.08}Mn_{0.27}]O_2$ Cathode Material with Full Concentration Gradient for Li-Ion Batteries. *J. Electrochem. Soc.* **2015**, *162*, A3059−A3063.
(14) Noh, H.-J.; Myung, S.-T.; Lee, Y. J.; Sun, Y.-K. High-Energy Layered Oxide Cathodes with Thin Shells for Improved Surface Stability. *Chem. Mater.* **2014**, *26*, 5973−5979.
(15) Cho, J.; Kim, T.-J.; Kim, J.; Noh, M.; Park, B. Synthesis, Thermal, and Electrochemical Properties of $AlPO_4$-Coated $Li-Ni_{0.8}Co_{0.1}Mn_{0.1}O_2$ Cathode Materials for a Li-Ion Cell. *J. Electrochem. Soc.* **2004**, *151*, A1899−A1904.
(16) Zheng, J.; Gu, M.; Xiao, J.; Polzin, B. J.; Yan, P.; Chen, X.; Wang, C.; Zhang, J.-G. Functioning Mechanism of AlF_3 Coating on the Li-and Mn-Rich Cathode Materials. *Chem. Mater.* **2014**, *26*, 6320−6327.
(17) Woo, S.-U.; Park, B.-C.; Yoon, C. S.; Myung, S.-T.; Prakash, J.; Sun, Y.-K. Improvement of Electrochemical Performances of $Li[Ni_{0.8}Co_{0.1}Mn_{0.1}]O_2$ Cathode Materials by Fluorine Substitution. *J. Electrochem. Soc.* **2007**, *154*, A649−A655.
(18) Woo, S. W.; Myung, S. T.; Bang, H.; Kim, D. W.; Sun, Y. K. Improvement of electrochemical and thermal properties of $Li-[Ni_{0.8}Co_{0.1}Mn_{0.1}]O_2$ positive electrode materials by multiple metal (Al, Mg) substitution. *Electrochim. Acta* **2009**, *54*, 3851−3856.
(19) Huang, B.; Li, X.; Wang, Z.; Guo, H.; Shen, L.; Wang, J. A comprehensive study on electrochemical performance of Mn-surface-modified $LiNi_{0.8}Co_{0.15}Al_{0.05}O_2$ synthesized by an in situ oxidizing-coating method. *J. Power Sources* **2014**, *252*, 200−207.
(20) Xiong, X.; Wang, Z.; Guo, H.; Zhang, Q.; Li, X. Enhanced electrochemical properties of lithium-reactive V_2O_5 coated on the $LiNi_{0.8}Co_{0.1}Mn_{0.1}O_2$ cathode material for lithium ion batteries at 60 °C. *J. Mater. Chem. A* **2013**, *1*, 1284−1288.
(21) Xiong, X.; Ding, D.; Bu, Y.; Wang, Z.; Huang, B.; Guo, H.; Li, X. Enhanced electrochemical properties of a $LiNiO_2$-based cathode material by removing lithium residues with $(NH_4)_2HPO_4$. *J. Mater. Chem. A* **2014**, *2*, 11691−11696.
(22) Chen, Y.; Zhang, Y.; Chen, B.; Wang, Z.; Lu, C. An approach to application for $LiNi_{0.6}Co_{0.2}Mn_{0.2}O_2$ cathode material at high cutoff voltage by TiO_2 coating. *J. Power Sources* **2014**, *256*, 20−27.
(23) Huang, Y.; Jin, F.-M.; Chen, F.-J.; Chen, L. Improved cycle stability and high-rate capability of Li_3VO_4-coated $Li[Ni_{0.5}Co_{0.2}Mn_{0.3}]-O_2$ cathode material under different voltages. *J. Power Sources* **2014**, *256*, 1−7.
(24) Lee, K.-S.; Myung, S.-T.; Amine, K.; Yashiro, H.; Sun, Y.-K. Structural and Electrochemical Properties of Layered $Li-[Ni_{1-2x}Co_xMn_x]O_2$ (x = 0.1 − 0.3) Positive Electrode Materials for Li-Ion Batteries. *J. Electrochem. Soc.* **2007**, *154*, A971−A977.
(25) Sun, Y.-K.; Noh, H.-J.; Yoon, C. S. Effect of Mn Content in Surface on the Electrochemical Properties of Core-Shell Structured Cathode Materials. *J. Electrochem. Soc.* **2011**, *159*, A1−A5.
(26) Hwang, B. J.; Tsai, Y. W.; Chen, C. H.; Santhanam, R. Influence of Mn content on the morphology and electrochemical performance of $LiNi_{1-x-y}Co_xMn_yO_2$ cathode materials. *J. Mater. Chem.* **2003**, *13*, 1962−1968.
(27) Sun, Y.-K.; Kang, H.-B.; Myung, S.-T.; Prakash, J. Effect of Manganese Content on the Electrochemical and Thermal Stabilities of $Li[Ni_{0.58}Co_{0.28-x}Mn_{0.14+x}]O_2$ Cathode Materials for Lithium-Ion Batteries. *J. Electrochem. Soc.* **2010**, *157*, A1335−A1340.
(28) Kim, H.-G.; Myung, S.-T.; Lee, J. K.; Sun, Y.-K. Effects of manganese and cobalt on the electrochemical and thermal properties of layered $Li[Ni_{0.52}Co_{0.16+x}Mn_{0.32-x}]O_2$ cathode materials. *J. Power Sources* **2011**, *196*, 6710−6715.
(29) Sun, Y.-K.; Myung, S.-T.; Kim, M.-H.; Prakash, J.; Amine, K. Synthesis and Characterization of $Li-[(Ni_{0.8}Co_{0.1}Mn_{0.1})_{0.8}(Ni_{0.5}Mn_{0.5})_{0.2}]O_2$ with the Microscale Core−Shell Structure as the Positive Electrode Material for Lithium Batteries. *J. Am. Chem. Soc.* **2005**, *127*, 13411−13418.
(30) Tan, L.; Liu, H. High rate charge−discharge properties of $LiNi_{1/3}Co_{1/3}Mn_{1/3}O_2$ synthesized via a low temperature solid-state method. *Solid State Ionics* **2010**, *181*, 1530−1533.
(31) Hwang, I.; Lee, C. W.; Kim, J. C.; Yoon, S. Particle size effect of Ni-rich cathode materials on lithium ion battery performance. *Mater. Res. Bull.* **2012**, *47*, 73−78.
(32) van Bommel, A.; Dahn, J. R. Analysis of the Growth Mechanism of Coprecipitated Spherical and Dense Nickel, Manganese, and Cobalt-Containing Hydroxides in the Presence of Aqueous Ammonia. *Chem. Mater.* **2009**, *21*, 1500−1503.
(33) Lin, F.; Markus, I. M.; Nordlund, D.; Weng, T.-C.; Asta, M. D.; Xin, H. L.; Doeff, M. M. Surface reconstruction and chemical evolution of stoichiometric layered cathode materials for lithium-ion batteries. *Nat. Commun.* **2014**, *5*, 3529.
(34) Hwang, S.; Chang, W.; Kim, S. M.; Su, D.; Kim, D. H.; Lee, J. Y.; Chung, K. Y.; Stach, E. A. Investigation of Changes in the Surface Structure of $Li_xNi_{0.8}Co_{0.15}Al_{0.05}O_2$ Cathode Materials Induced by the Initial Charge. *Chem. Mater.* **2014**, *26*, 1084−1092.
(35) Zheng, J.; Xu, P.; Gu, M.; Xiao, J.; Browning, N. D.; Yan, P.; Wang, C.; Zhang, J.-G. Structural and Chemical Evolution of Li- and Mn-rich Layered Cathode Material. *Chem. Mater.* **2015**, *27*, 1381−1390.
(36) Nobili, F.; Croce, F.; Scrosati, B.; Marassi, R. Electronic and Electrochemical Properties of $Li_xNi_{1-y}Co_yO_2$ Cathodes Studied by Impedance Spectroscopy. *Chem. Mater.* **2001**, *13*, 1642−1646.
(37) Zheng, J.; Wu, X.; Yang, Y. Improved electrochemical performance of $Li[Li_{0.2}Mn_{0.54}Ni_{0.13}Co_{0.13}]O_2$ cathode material by fluorine incorporation. *Electrochim. Acta* **2013**, *105*, 200−208.
(38) Kang, Y. J.; Kim, J. H.; Lee, S. W.; Sun, Y. K. The effect of $Al(OH)_3$ coating on the $Li[Li_{0.2}Ni_{0.2}Mn_{0.6}]O_2$ cathode material for lithium secondary battery. *Electrochim. Acta* **2005**, *50*, 4784−4791.
(39) Zheng, J.; Shi, W.; Gu, M.; Xiao, J.; Zuo, P.; Wang, C.; Zhang, J.-G. Electrochemical Kinetics and Performance of Layered Composite Cathode Material $Li[Li_{0.2}Ni_{0.2}Mn_{0.6}]O_2$. *J. Electrochem. Soc.* **2013**, *160*, A2212−A2219.

DOI: 10.1021/acsami.5b00788
ACS Appl. Mater. Interfaces 2015, 7, 6926−6934